Polymer 51 (2010) 4790–4805

Contents lists available at ScienceDirect

Polymer

journal homepage: www.elsevier.com/locate/polymer

Dielectric analysis of poly(methyl methacrylate) zinc(II) mono-pinacolborane diphenylporphyrin composites

Brent Hilker, Kimberly B. Fields, Abraham Stern, Brian Space, X. Peter Zhang, Julie P. Harmon*

Department of Chemistry, University of South Florida, 4202 E. Fowler Avenue, Tampa, FL 33620-5250, United States

ARTICLE INFO

Article history:
Received 21 May 2010
Received in revised form
11 August 2010
Accepted 21 August 2010
Available online 16 September 2010

Keywords:
Dielectric analysis (DEA)
Polymer Composite
Degradation

ABSTRACT

Poly(methyl methacrylate) (PMMA) composites were made from a polar metalloporphyrin [5-(4′,4′,5′,5′-tetramethyl[1′,3′,2′]dioxaborolan-2′-yl)-10,20-diphenylporphyrinato]zinc(II) (Zn(II)Bpin-DPP) in select weight % (wt%). Differential Scanning Calorimetry (DSC) showed that porphyrin acted as an anti-plasticizer raising the glass transition (Tg) from 105 °C to 123 °C. Dielectric Analysis (DEA) was performed in the frequency range of 0.3 Hz to 100 kHz between −150 and 270 °C. Permittivity (ε'), loss factor (ε'') and dielectric response of beta (β), alpha beta (αβ), and conductivity relaxations were studied. Previous DEA data was limited to 190 °C. This study brings analysis to 270 °C which is start point for the first part of PMMA degradation. Thus forwarding DEA can be used to evaluate PMMA degradation. The electric modulus formalism is used to reveal the β and conductivity relaxations. The apparent activation energies (E_a) for the molecular relaxations are presented. AC (σ_{AC}) and DC (σ_{DC}) conductivity are also evaluated.

1. Introduction

The purpose of this investigation is to understand the structure–property relations of metalloporphyrin-containing polymers because metalloporphyrins are of current interest in sensors, sequestration, and destruction of target analytes. Recent advancements by Zhang's group have led to new synthetic routes and functionalities of porphyrins [1–10]. This has led to an impressive novel library of functionalized porphyrins with the ability to provide additional custom porphyrins and corroles for specific applications. Currently, there is a dearth of information about the interactions and structure–property relations of porphyrins in polymer systems.

Dielectric spectroscopy provides information about the segmental mobility of a polymer [11]. Polymers that have repeating units whose dipole vector summation accumulates can be studied via Dielectric Analysis (DEA). Different conformational states of the polymer can be studied via this method. When DEA is performed upon polymer composites, interactions between the filler and polymer can be better understood. To obtain quality DEA spectroscopy the polymer and filler materials must possess a permanent or inducible dipole [12].

Typically, DEA is performed by subjecting a sample to an alternating electric field while placed between a parallel plate capacitor. The sample will then be subjected to a discrete temperature range and frequency sweep. The dielectric constant (permittivity ε') and dielectric loss (loss factor ε'') are measured as a function of time, temperature, and frequency. These measurements allow for the examination of specific segmental relaxations by analysis of the different maxima observed. The molecular relaxations by convention start their assignment sequentially, from high to low temperature, with alpha (α), then beta (β), gamma (γ), and so forth.

The α relaxation is associated with the glass transition (Tg) of the polymer and is attributed to the main chain translation (backbone) [11]. The α relaxation can manifest in five possible scenarios that are well described by Garwe et al. [13]. From these five scenarios the α relaxation can be determined using Arrhenius plots (natural log (ln) frequency versus inverse temperature). Arrhenius plots may be linear or nonlinear. Nonlinear plots can be curve fitted using the Vogel Fulcher Tamman (VFT) or Williams–Landel–Ferry (WLF) laws [14,15]. The α relaxation Arrhenius plots obtained from DEA also can be linear revealing apparent activation energy (E_a) [16–20]. Whether the Arrhenius plot is linear or nonlinear depends upon several factors that occur when the αβ cooperative relaxations manifest their split. The reader is directed to explore reference [13] by Garwe et al. for further detail.

Subsequent relaxations (β and γ) occur below the Tg and are specific to the moieties of each polymer tested representing rotational reorientation from the applied electric field. These sub-Tg (lower temperature) relaxations characteristically exhibit linear behavior in Arrhenius DEA plots [11,21].

Individual relaxations can become more complex when constructive or destructive cooperation manifests. The merging of different

* Corresponding author. Tel.: +1 813 974 3997; fax: +1 813 974 1733.
E-mail address: harmon@cas.usf.edu (J.P. Harmon).

0032-3861/$ – see front matter © 2010 Elsevier Ltd. All rights reserved.
doi:10.1016/j.polymer.2010.08.049

molecular relaxations commonly occurs, for example an αβ merge [17–20,22–26]. This results when the two separate molecular relaxations have sufficient overlap in the DEA spectrum and their reorientation to the applied electric field is in resonance or cooperative.

Conductivity relaxations occur at temperatures significantly above the Tg. Aptly, the temperature region in which this occurs is called the conductivity region. This region is significant because the polymer exhibits minimal viscoelastic effects allowing the researcher to obtain alternating (AC) and direct current (DC) conductivities as well as their respective activation energies for ion translation [21,22,27,28].

Poly(methyl methacrylate) (PMMA) has been widely studied via DEA and offers a great starting point for the first full investigation of porphyrin–PMMA composite molecular interactions [13,16,18–20,22,24,25,29–33].

PMMA generally has two dielectrically active relaxations, α and β, and a conductivity relaxation. The α relaxation is attributed to the main chain (backbone) translation slippage [11]. The α relaxation is weak in PMMA and generally merges with the fast strong β relaxation. The β relaxation corresponds to the motion of the [(C═O)OCH_3] side groups attached to the main chain [32]. Note that for pure PMMA, the γ relaxation, ($-CH_3$), has not yet been observed using DEA. The γ relaxation is not typically observed with DEA because the ($-CH_3$) moiety is not significantly polarizable [29,32]. However, it is possible to observe the γ relaxation of PMMA composites when the local environment permits such cooperation whereas to make the ($-CH_3$) sufficiently polarizable. Our group has observed the electrically active γ relaxation of PMMA-carbon nanotube composites [24].

Porphyrins have been of great interest to chemists and engineers in recent times because they have been shown to be very useful in various areas such as dye sensitized solar cells (DSSCs), catalysis, polymer light emitting diodes (PLEDs), and light harvesting [34–38]. Recently, porphyrins have become the interest of this group because of their potential ability to sequester nerve agents, choking agents, and biological agents for later photocatalytic destruction.

In this study, dielectric analysis enabled the exploration into the interaction of a metalloporphyrin, [5-(4',4',5',5'-tetramethyl[1',3',2']dioxaborolan-2'-yl)-10,20-diphenylporphyrinato]zinc(II), (Zn(II)Bpin-DPP), with PMMA. In the literature there is a lack of DEA information with respect to the interactions of porphyrins with polymeric systems. Furthermore, DEA performed upon PMMA generally stops at temperatures (<190 °C) before the first of a two part degradation process which begins at *ca.* 220 °C. To our knowledge, this is the first study to both probe the complete dielectric interactions of a porphyrin–polymer composite system as a function of time, temperature, and frequency while testing thermally beyond the first of a two part degradation process.

2. Synthesis of polymer–porphyrin composites

2.1. Experimental materials

The methyl methacrylate (MMA) monomer was purchased from Aldrich (Milwaukee, WI), and the 2,2′-azobis(2,4-dimethylpentane nitrile) (VAZO 52®) initiator was purchased from DuPont (Wilmington, DE). The solvents used, including reagent grade dichloromethane (CH_2Cl_2) and reagent grade methanol (MeOH), were purchased from Fisher Scientific (Pittsburgh, PA). The monomethyl ether hydroquinone (MEHQ) inhibitor was removed from the MMA using a fresh MEHQ inhibitor remover column available from Aldrich (Milwaukee, WI). All other materials were used without further purification. Fresh 30 g columns were packed with Aldrich HQ/MEHQ Inhibitor remover (CAS 9003-70-7). These 30 g columns can remove 100 ppm HQ/MEHQ from 3 L of MMA monomer, which contains 10–100 ppm HQ/MEHQ inhibitor. 50 mL of monomer were purified ensuring all inhibitor was removed.

2.2. Synthesis of zinc monoborate diphenyl porphyrin (Zn(II) Bpin-DPP)

[5-(4',4',5',5'-tetramethyl[1',3',2']dioxaborolan-2'-yl)-10,20-diphenylporphyrinato]zinc(II) (zinc monoborate diphenylporphyrin) (Zn(II)Bpin-DPP) was synthesized by following the synthesis set forth by Hyslop et al. ^{1}H NMR and UV–vis spectra were obtained to confirm the synthesis of the Zn(II)Bpin-DPP molecule [39].

^{1}H NMR (400 MHz, $CDCl_3$, δ): 10.28 (s, 1H, meso-H), 9.94 (d, $J = 4.8$ Hz, 2H, βH), 9.39 (d, $J = 4.4$ Hz, 2H, βH), 9.12 (d, $J = 4.8$ Hz, 2H, βH), 9.06 (d, $J = 4.8$ Hz, 2H, βH), 8.23 (d, $J = 1.6$ Hz, 2H, H-Ph), 8.22 (d, $J = 2.0$ Hz, 2H, H-Ph), 7.78 (m, 6H, H-Ph), 1.85 (s, 12H, –O–C$(CH_3)_2$–C$(CH_3)_2$–O–) UV–vis Zn(II) BPin-DPP (CH_2Cl_2): λ_{max} (log ε) = 391 (4.67), 411 (5.71), 506 (3.60), 540 (4.29), 573 (3.57) nm.

2.3. Poly(methyl methacrylate) synthesis

Poly(methyl methacrylate) (PMMA) was synthesized via radical chain polymerization. 0.2 wt% of the initiator, 2,2′-azobis [2,4-dimethylvaleronitrile], was added to and dissolved in deinhibited methyl methacrylate monomer. The solution was polymerized in bulk at 60 °C for 18 h under an inert atmosphere of N_2 gas inside a scintillation vial. The low polymerization temperature ensured an even polymerization and bubble free samples were obtained. High molar mass polymer was verified using DSC showing high Tg, Section 2.5.4. The resulting polymer was then dissolved in CH_2Cl_2 and then precipitated in methanol to remove any impurities and dried under vacuum at 110 °C for 48 h.

2.4. PMMA(Zn(II)Bpin-DPP) composite synthesis

Four samples were made for DEA experimentation. A control, PMMA, and 3 different weight percents (wt%) (w/w) (0.05, 0.11, 0.9) were made by dissolving the polymer and dye in CH_2Cl_2, pouring the solutions into scintillation vials, and then removing the solvent via a vacuum oven at 80 °C for 48 h. Scintillation vials were broken to remove the samples. Samples were then molded in a Carver press as described in Section 2.5.3.

2.5. Instrumentation

2.5.1. H^1NMR

A Varian Inova 400 MHz NMR spectrometer was used to obtain ^{1}H NMR spectra of the porphyrin molecule.

2.5.2. UV/VIS spectroscopy

A Perkin Elmer Lambda 40 spectrophotometer was used to obtain spectra on four separate molar concentrations of Zn(II)Bpin-DPP in CH_2Cl_2. The four samples were made to ensure that the greatest maximum absorbance of the Sorret band was below 1.2. From these spectra the molar extinction coefficient, ε, of the Sorret band (410.5 nm) and secondary bands were calculated. These values are listed in Section 2.2 and analysis is offered in Section 3.2.

2.5.3. Sample molding

Samples were compression molded using a Carver Press (Wisconsin, USA) equipped with a heating element at a temperature of 160 °C at a pressure of 13,788 kPa (2000 psi) to the dimensions of 25 mm × 21.5 mm × 0.6 mm. Samples were held at these conditions for 10 min and then cooled to room temperature. Samples were then stored under vacuum at 50 °C until ready for DEA

analysis, Fig. 1b. Samples were optically transparent under microscope (500×) showing no visible agglomeration.

2.5.4. Differential scanning calorimetry DSC

A TA Instruments 2920 DSC instrument was used to calculate the glass transition temperature (Tg) of the PMMA control and PMMA composites. PMMA and composite samples mass ranged from 5 to 10 mg and were placed in an open aluminum pan. An inert environment was created in the cell using N_2 at a flow rate of 60–70 mL/min. Samples were first equilibrated at 30 °C and held isothermal for 2 min then scanned at a rate of 7 °C/min up to 150 °C. All samples were air cooled in the same manner by removing the heat source and equilibrating at ambient temperature for 15 min at 20 °C. Sample data was taken on the second run in order to remove any thermal history following the same procedure.

2.5.5. Dielectric analysis (DEA)

Dielectric analysis was performed using a TA Instruments DEA 2970. The sample was heated to 150 °C and then taken down to the cryogenic temperature of −150 °C. A TA single surface sensor was employed where a maximum force of 250 N was applied to achieve the minimum spacing of 0.30 mm. Measurements were taken in 5 °C increments from −150 to 270 °C. Frequencies tested ranged from 0.3 Hz to 100 kHz. The measurements were taken under an inert argon atmospheric purge of 600 mL/min. Capacitance and conductance were measured as a function of time, temperature, and frequency to obtain the dielectric constant, permittivity (ε'), and the dielectric loss (ε'').

3. Results

3.1. Dipole moment Zn(II)Bpin-DPP

Because DEA works by detecting permanent or inducible dipoles, a computational calculation of the electronics of Zn(II) Bpin-DPP was performed and presented.

Calculation of the dipole was performed using Gaussian03 [40] on an SGI Altix through the Teragrid [41] and using Gamess [42] at University of South Florida's Research Computing. All calculations were performed using density functional theory (DFT). Results obtained from DFT can depend on the choice of functional. As such, care was taken in selecting functionals and basis sets appropriate for the calculations performed. Additionally, comparisons were made between several choices of basis sets and density functional. The structure was first optimized using the B3LYP density functional and a 6-31G* basis set. The dipole moment of the optimized structure, computed at the same level of theory, was found to be 2.63 Debye. A density functional that has been developed specifically for calculations involving transition metals, the M06-L functional, a local functional, was also employed for comparison [43]. The structure was reoptimized using the M06-L density functional with the LANL2TZ basis set on the zinc center and 6-31G* on the rest of the atoms. The M06-L functional resulted in a dipole of 2.87 Debye. A final comparison is made to the dipole calculated using the M06 functional, recommended for use in calculations involving organometallic systems [43,44]. Using the M06 functional in conjunction with the LANL2TZ/6-31G* mixed basis set detailed above resulted in a dipole of 2.77 Debye for the optimized geometry. All three computed dipoles are in good qualitative agreement. In all cases, the dipole points along a vector drawn from the zinc center of the porphyrin to the boron-containing substituent. This is the conventional definition of the dipole moment in which the vector is taken to point from negative to positive charge density. In Fig. 2a Zn(II)Bpin-DPP structure is provided along with the optimized structure in Fig. 2b.

As a point of reference, Table 1 lists Zn(II)Bpin-DPP along with a few common solvents with their permanent dipoles values in Debyes.

3.2. UV–vis spectroscopy

UV–vis spectra obtained, Fig. 3, show a Sorret band at 410.5 nm which contains a left shoulder at 391 nm. A secondary peak is observed at 540 nm flanked on each side by shoulders at 506 and 572.5 nm. The UV–vis spectrum confirms the presence of the metalloporphyrin revealing one Sorret band and a single secondary peak [45]. In contrast, free base porphyrins that do not contain metal ions characteristically contain one Sorret band with 4 Q-bands occurring at higher wavelengths [45].

3.3. DSC data

DSC data was obtained for the PMMA control and PMMA-Zn(II) Bpin-DPP composite samples. The glass transition temperature (Tg) was shown to increase slightly with increasing wt% (w/w). The Tg temperatures for samples tested are listed in Table 2. The observed increase in Tg reveals that Zn(II)Bpin-DPP may be acting as an antiplasticizer.

3.4. Dielectric analysis (DEA)

In DEA, the material is exposed to an alternating electric field generated by an applied sinusoidal voltage. The applied electric field causes the alignment or induction of dipoles in the material which results in polarization. Since both the polymer (PMMA) and the dye (Zn(II)Bpin-DPP) possess a permanent dipole moment, DEA can measure two fundamental characteristics of the composite: capacitance and conductance as $f(t, T, f)$ [12]. The capacitive nature of the material is its ability to store electrical charge while the conductive nature is the material's ability to transfer electric

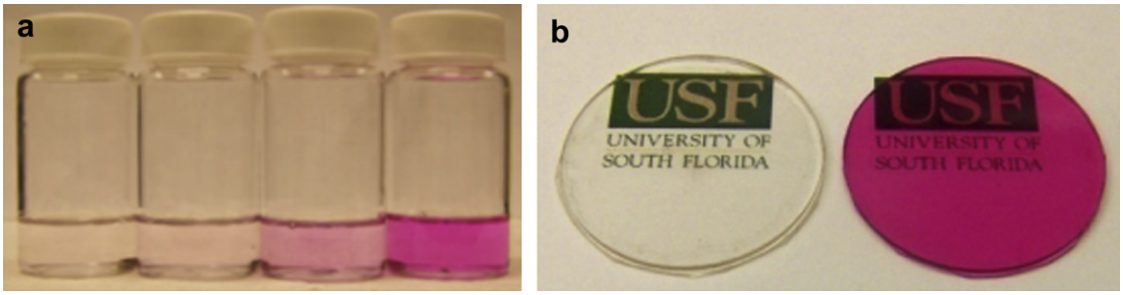

Fig. 1. (a) Poly(methyl methacrylate) control, 0.05, 0.11 and 0.9 wt% Zn(II)Bpin-DPP samples prepared for solution casting. (b) Carver thermal pressed samples (control and 0.11 wt% composite).

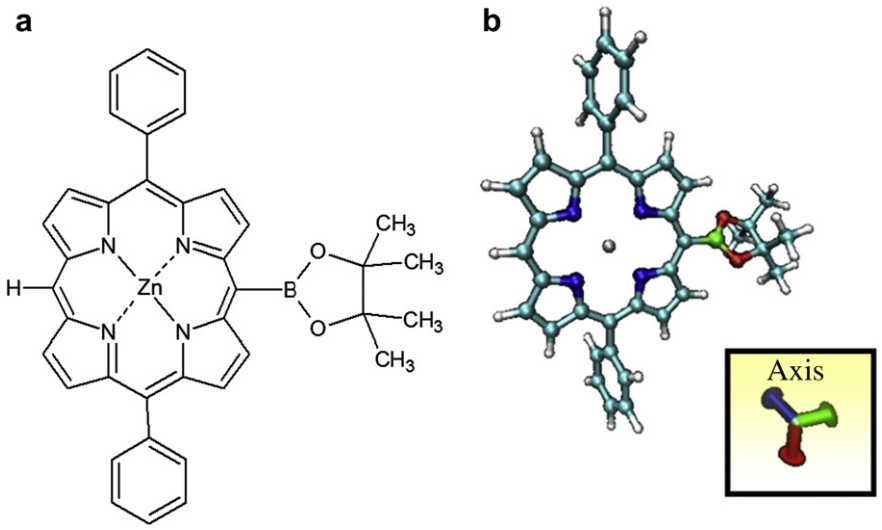

Fig. 2. (a) Structure of Zn(II)Bpin-DPP and (b) 3-D geometry optimized structure of Zn(II)Bpin-DPP as computed at the B3LYP/6-31G* level of theory with inset (x, y, z) orientation guide.

charge. One feature of DEA is that this spectroscopy allows for the investigation of molecular mobility, or relaxations of the material.

The complex permittivity, ε^*, of a system is defined [21].

$$\varepsilon^* = \varepsilon' - i\varepsilon''$$

$$\varepsilon' = \varepsilon'_{\text{induced dipole}} + \varepsilon'_{\text{allignment of dipole}}$$

$$\varepsilon' = \varepsilon'_{\text{dipole loss factor}} + \varepsilon'_{\text{ionic conductance}}$$

where ε' is the real part of the complex relative permittivity (dielectric constant) and represents the amount of dipole alignment both induced and permanent. ε'' is the dielectric loss (loss factor) and represents the dipole loss factor plus ionic conduction.

The classic Debye equation (eq. (1)) was introduced to account for dielectric effects on dilute polar solutions [46,47]. McCrum et al. [21] separated the real and imaginary components of the classic Debye equation obtaining ε' and ε'' (eqs. (2) and (3)) which were later modified to account for ionic conductivity as follows [12]:

$$\varepsilon^* = \varepsilon_\infty + \frac{\Delta\varepsilon}{1 + i\omega^2\tau^2} \tag{1}$$

$$\varepsilon' = \varepsilon_\infty + \frac{\Delta\varepsilon}{1 + \omega^2\tau^2} \tag{2}$$

$$\varepsilon'' = \Delta\varepsilon\frac{\omega\tau}{1 + \omega^2\tau^2} + \frac{\sigma}{\omega\varepsilon_0} \tag{3}$$

$$\varepsilon''_{\text{ion}} = \frac{\sigma_{\text{AC}}}{\omega\varepsilon_0} \tag{4}$$

Table 1
Dipole moment of Zn(II)Bpin-DPP compared with common solvents.

Solvent	Dipole moment (Debye)
Methanol	1.7
Water	1.85
Zn(II)Bpin-DPP	2.87
Acetone	2.88
Acetonitrile	3.92

$\Delta\varepsilon$: relaxation strength ($\Delta\varepsilon = \varepsilon_S - \varepsilon_\infty$)
ε_S: static dielectric permittivity at zero frequency
ε_∞: dielectric permittivity at high frequency
ω: angular frequency ($2\pi f$)
σ: ionic conductivity
ε_0: absolute permittivity of free space (8.854×10^{-14} F/cm)

3.4.1. Permittivity

The permittivity of a dielectric material is measured relative to that of a vacuum ($\varepsilon_0 = 8.85 \times 10^{-12}$ Fm^{-1}) [48]. ε', permittivity (dielectric constant), was shown to increase with increasing porphyrin content. ε' represents the amount of dipole alignment both induced and permanent within the sample. Permittivity was observed to increase with increasing temperature. Fig. 4a and b shows permittivity for 70 °C and 25 °C, respectively.

The permittivity increases to maximum amount when 0.11 wt% of Zn(II)Bpin-DPP was added. There was no observed increase in the composite material's permittivity when loading was beyond 0.11 wt%. At 25 °C, a decrease in permittivity could be observed at frequencies above *ca.* 600 Hz for the 0.9 wt% sample. In comparison, at 70 °C the 0.11 wt% and 0.9 wt% samples achieved the maximum observed permittivity. From these observations, it appears the PMMA-Zn(II)Bpin-DPP composites reach a maximum loading capacity *ca.* 0.11 wt% of Zn(II)Bpin-DPP for STP conditions. The noted decrease in permittivity that appears at 25 °C (above 600 Hz), but disappears at 70 °C is explainable by considering the added thermal energy within the system. As the thermal energy rises there is an increase in the free volume of the composite allowing for the greater reorientation of dipoles in the composite in response to the applied electric field. Since only the higher frequencies tested (600 Hz to 100 kHz) showed the decrease, it is possible that the composite was above the maximum loading capacity with respect to permittivity increase. Therefore, this sample had the porphyrin packed tightly neither affording the proper free volume nor the time to allow for reorientation to the applied electric field.

3.4.2. Electric modulus

McCrum et al. showed that by inverting the complex permittivity one could obtain the complex electric modulus (eq. (5)) [21]. Ambrus, Moynihan, and Macedo were the first to publish the electric modulus for the investigation of electrical relaxation phenomena in vitreous ionic conductors [27].

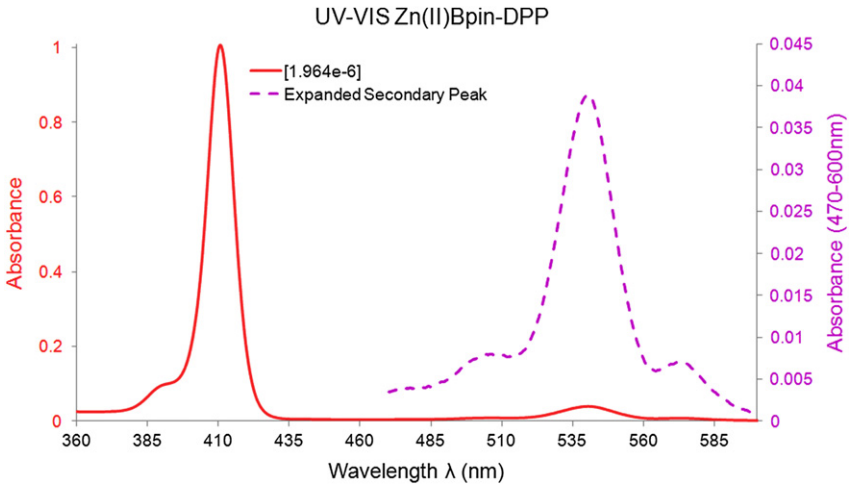

Fig. 3. UV–vis spectrum of 1.964×10^{-6} M solution Zn(II)Bpin-DPP in CH_2Cl_2. The right secondary *y*-axis corresponds to the expanded view of the absorbance peak upon 540 nm.

$$M^* = \frac{1}{\varepsilon^*} = M' + iM'' = \frac{\varepsilon'}{\varepsilon'^2 + \varepsilon''^2} + i\frac{\varepsilon''}{\varepsilon'^2 + \varepsilon''^2} \quad (5)$$

M^*: complex electric modulus
M': electric storage modulus
M'': electric loss modulus

The electric modulus formalism is particularly useful when applied to dielectric spectra of polymers and polymer composites. Polymers and polymer composite systems contain interfacial polarization, also known as the Maxwell–Wagner–Sillars (MWS) effect [49–51]. The MWS effect is present because fillers, additives, and even impurities can create a heterogeneous system. In systems that contain conductive components interfacial relaxation can be obscured by the conductivity, essentially masking targeted molecular relaxations. Employment of the electric modulus reveals the relaxations obscured by ionic conductivity by subtracting the conductivity effects and revealing the molecular relaxations.

3.4.3. β and αβ Arrhenius trace

Plotting Arrhenius diagrams for the $\varepsilon''(\omega)$ peak maximum frequencies (ω_{max}) the β and αβ trace become visually distinguished. All samples tested appear to maintain "c" type character as reported by Garwe et al. [13] Garwe et al. detail that the "c" type character to consist of a locally coordinative β precursor at higher temperatures that prepares the cooperative αβ process. The cooperative αβ process deviates from linear behavior and manifests as a nonlinear curves as seen in Fig. 5a–d, and is discussed later. Additionally, below the α onset temperature, a simpler β process remains which exhibits linear characteristics.

These Arrhenius diagrams can also be plotted using the electric modulus, $M''(\omega_{max})$, Fig. 6a–d. In these plots it is not inherently obvious as to where the β and αβ relaxations manifest, but greater clarity of the simple β relaxation is seen. It can be seen in these trace plots that at higher frequencies of 30–100 kHz a nonlinear character begins to emerge. In order to effectively identify the end of the simple β process and beginning of the αβ process a careful inspection of the peak widths must be entailed. Even with performing such an analysis the nonlinear behavior of the αβ merge can be obfuscated when using the $M''(\omega_{max})$ versus inverse temperature. Furthermore, the employment of the electric modulus formalism is known to make significant changes in plots

Table 2
DSC glass transition (Tg) temperatures (°C) for PMMA and PMMA-Zn(II)Bpin-DPP composites at respective wt%.

Sample	Tg (°C)
PMMA	105.2
0.05 wt%	119
0.11 wt%	119.9
0.9 wt%	123

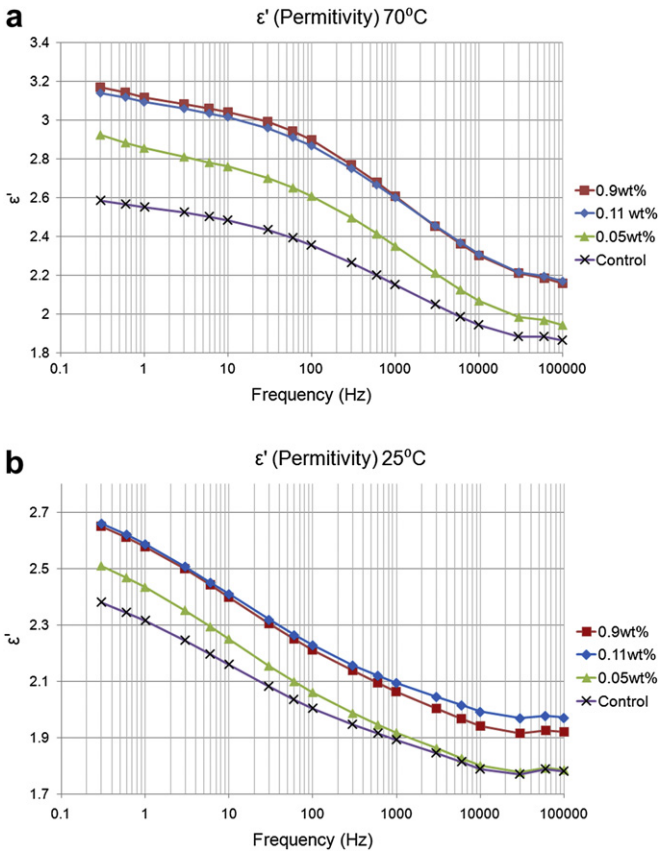

Fig. 4. Permittivity (ε') versus frequency (Hz) for (a) 70 °C and (b) 25 °C.

that differ from those created with the loss factor, ε'' [22,23]. Differences include: maxima shifted to lower temperature than ε'' peaks, and separation of visocelastic and conductivity relaxations. Although these differences exist, the electric modulus formalism as shown here reproduces the same data when analyzed and is invaluable to the exploration into the conductivity relaxations in polymer composites [22,23].

3.4.4. β relaxation

The beta (β) relaxations are visible in both plots of ε'' and M'' versus temperature whereas the conductivity relaxations are obscured by MWS effect. The conductivity relaxations only become visible in the M'' versus T plots, Fig. 7a–d, and are discussed later. Notice the clarity of the β relaxation plots in the M'' plots compared to the ε'' plots, Fig. 7b and d. This relaxation is attributed to the motion of the [(C═O)OCH_3] side groups attached to the main chain [32]. PMMA is unique in that it has a large temperature range in which this relaxation occurs when compared to other polymers. This relaxation obeyed Arrhenius behavior which is characteristic of secondary relaxations in polymers. Arrhenius plots of ln frequency versus the reciprocal of temperature were created where the slope was used to generate the apparent activation energy, E_a, utilizing the following equation (eq. (6)) [11,21].

$$\ln f = \ln f_0 - \frac{\Delta E_a}{RT} \tag{6}$$

The apparent activations energies were calculated two ways for comparison. The first method was constructed using the loss factor, ε'', plots. The apparent activation energy, E_a, was evaluated with Arrhenius plots of ln f_{max} ($\varepsilon''(\omega_{max})$) versus inverse temperature. The second method was similar, but involved the use of the electric modulus formalism to obtain electric loss modulus, M'', versus inverse temperature plots. The second method obtained the apparent E_a using Arrhenius plots of ln f_{max} ($M''(\omega_{max})$) versus inverse temperature. It is the intent to compare the two methods and highlight their similarities and differences.

3.4.5. β relaxation via $\varepsilon''(\omega_{max})$

It was observed with ε'' plots that β relaxation maxima occurred 0.3–1000 Hz (2–85 °C) for PMMA; 0.3–300 Hz (0.8–65 °C) for PMMA-Zn(II)Bpin-DPP 0.05 wt%; 0.3–300 Hz (4.8–65 °C) for PMMA-Zn(II)Bpin-DPP 0.11 wt%; and 0.3–300 Hz (−3.4–61 °C) for PMMA-Zn(II)Bpin-DPP 0.9 wt%. Table 3 lists max peak temperature at 300 Hz, the highest frequency simple β relaxation shared amongst all samples. This shows the simple β $\varepsilon''(\omega_{max})$ peak at 300 Hz to decrease with increasing porphyrin content. The additional loading of Zn(II) Bpin-DPP trends the observed maxima to lower temperatures and brought upon αβ relaxational merging at lower frequencies from 3000 Hz to 300 Hz. The apparent E_a of the β relaxation utilizing this method are
listed in Table 4. The apparent E_a obtained for PMMA 78.22 kJ mol^{-1} (18.69 kcal mol^{-1}), PMMA-Zn(II)Bpin-DPP 0.05 wt% 81.1 kJ mol^{-1} (19.4 kcal mol^{-1}), PMMA-Zn(II)Bpin-DPP 0.11 wt% 81.47 kJ mol^{-1} (19.47 kcal mol^{-1}), and PMMA-Zn(II)Bpin-DPP 0.9 wt% 77.6 kJ mol^{-1} (18.5 kcal mol^{-1}) allows for the conclusion that the apparent E_a for the β relaxation seems to remain unaffected by the porphyrin at these wt%.

3.4.6. β relaxation via M''

The employment of the electric modulus formalism showed the well documented shift of peak maxima to lower temperatures

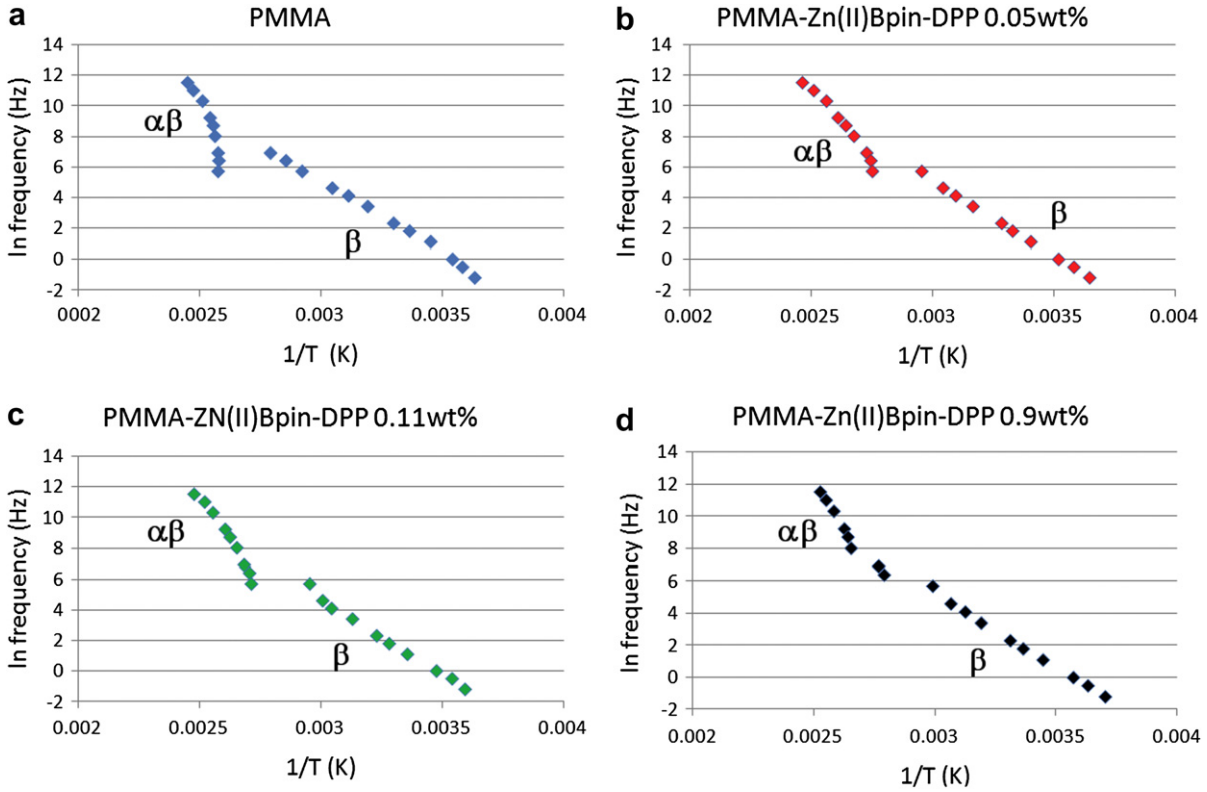

Fig. 5. Arrhenius plots $\varepsilon''(\omega_{max})$ versus 1/T (K) showing αβ and β divergence for (a) PMMA, (b) PMMA-Zn(II)Bpin-DPP 0.05 wt%, (c) PMMA-Zn(II)Bpin-DPP 0.11 wt%, and (d) PMMA-Zn(II)Bin-DPP 0.9 wt%.

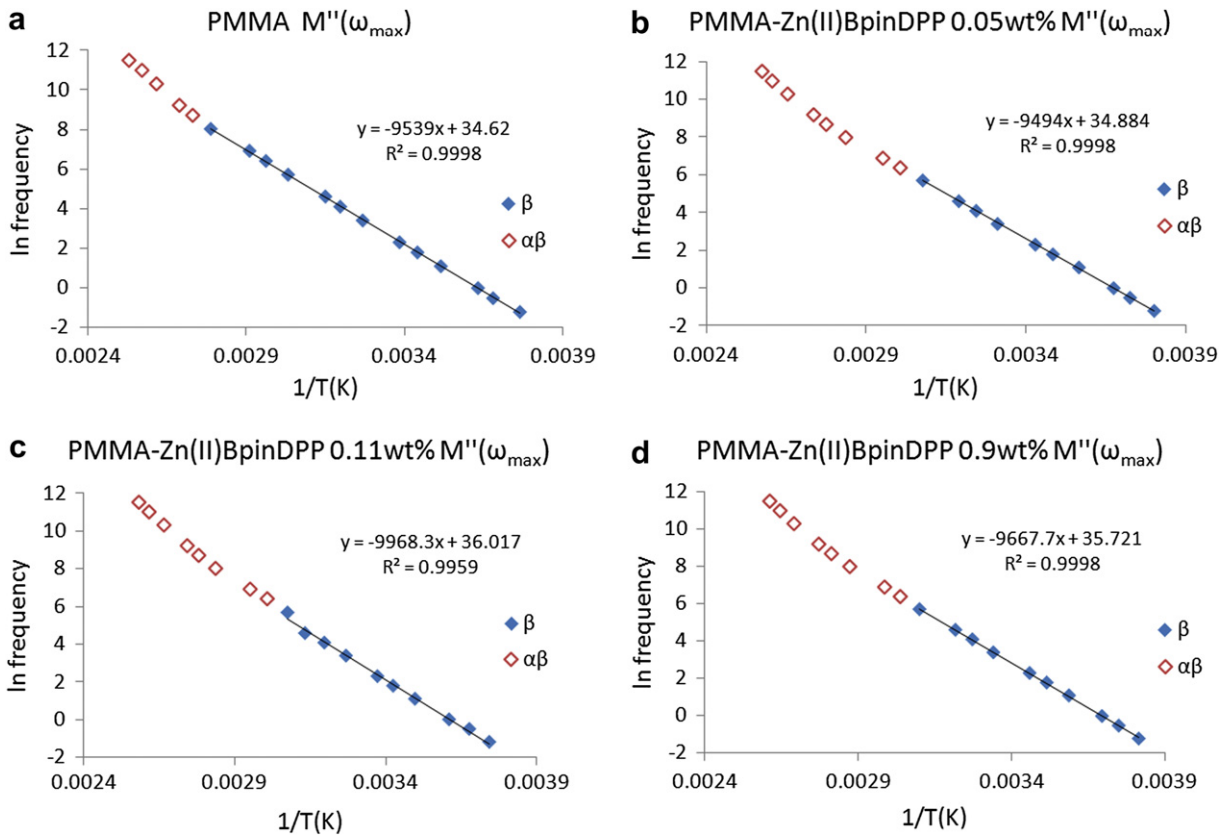

Fig. 6. Arrhenius plots $M''(\omega_{max})$ versus 1/T (K) showing αβ and β relaxations for (a) PMMA, (b) PMMA-Zn(II)Bpin-DPP 0.05 wt%, (c) PMMA-Zn(II)Bpin-DPP 0.11 wt%, and (d) PMMA-Zn(II)Bpin-DPP 0.9 wt%.

when compared to ε'' method [22,23]. M'' plots revealed β relaxation maxima located at: 0.3–1000 Hz (−7.4–70.4 °C) for PMMA; 0.3–300 Hz (-10–52.0 °C) for PMMA-Zn(II)Bpin-DPP 0.05 wt%; 0.3–300 Hz (−5.9–52.0 °C) for PMMA-Zn(II)Bpin-DPP 0.11 wt%; and 0.3–300 Hz (−10.9–49.3 °C) for PMMA-Zn(II)Bpin-DPP 0.9 wt%.

Table 3 lists max peak temperature at 300 Hz for $M''(\omega_{max})$, the same trend of decreasing peak maxima $M''(\omega_{max})$ with increasing porphyrin content as was calculated using $\varepsilon''(\omega_{max})$. The difference is the shift of these maxima to lower temperatures using M''.

The apparent E_a of the β relaxation utilizing this M'' are listed in Table 4. The apparent E_a obtained for PMMA 79.31 kJ mol^{-1} (18.95 kcal mol^{-1}), PMMA-Zn(II)Bpin-DPP 0.05 wt% 78.93 kJ mol^{-1} (19.4 kcal mol^{-1}), PMMA-Zn(II)Bpin-DPP 0.11 wt% 81.47 kJ mol^{-1} (19.47 kcal mol^{-1}), and PMMA-Zn(II)Bpin-DPP 0.9 wt% 77.6 kJ mol^{-1} (18.5 kcal mol^{-1}). Although the shift of the maxima occur at lower temperatures the information obtained from the M'' and ε'' methods are in agreement.

The apparent E_a of the β relaxation varied slightly in each sample, but the addition of the porphyrin dye appeared to have no appreciable effect upon the apparent β E_a. Therefore, the addition of the Zn(II)Bpin-DPP had no influence upon the rotation of the [(C=O)OCH_3] group. Thus alternatively arriving at the conclusion showing the apparent E_a for the β relaxation seems to remain unaffected by the porphyrin loading at the tested wt%. Furthermore, literature values for the β relaxation for PMMA generally range between 71 and 84 kJ mol^{-1} (17–20 kcal mol^{-1}) [17,19–21,24,25,29,32]. The values obtained in this study 78.2–79.3 kJ mol^{-1} (18.7–18.9 kcal mol^{-1}) are in agreement with previous studies.

3.4.7. PMMA αβ merge

Viewing the loss factor, ε'', versus temperature plots in Fig. 7a and c the αβ merge is observed. The Arrhenius plots of the αβ merge are nonlinear, Fig. 5a–d. The αβ merge was observed for PMMA 3–100 kHz (116–135 °C); PMMA-Zn(II)Bpin-DPP 0.05 wt% 1–100 kHz (89–132 °C); PMMA-Zn(II)Bpin-DPP 0.11 wt% 3–100 kHz (95–130 °C); PMMA-Zn(II)Bpin-DPP 0.9 wt% 3–100 kHz (103–122 °C). The onset of the αβ merge was shifted to lower temperatures with increasing porphyrin content. Comparative αβ relaxation frequency maxima across the samples had their maxima shifted slightly towards lower temperatures, commensurate with increased porphyrin loading. Table 5 lists the $\varepsilon''(\omega_{max})$ frequencies shared in the αβ merge relaxation region indicating that the increased porphyrin content shifts this cooperative relaxation towards lower temperatures.

The Vogel–Fulcher equation, (eq. (7)) was used to fit the nonlinear αβ merge plot of the relaxation time $\tau_{\alpha\beta}$ of the αβ merge in PMMA and PMMA-Zn(II)Bpin-DPP composites [52].

$$\tau_{\alpha\beta} = \tau_0 \exp\frac{DT_0}{T - T_0} \tag{7}$$

$\tau_{\alpha\beta}$: αβ merge relaxation time (s^{-1})
τ_0: extrapolated relaxation time at infinite temperature.
T_0: temperature where extrapolated relaxation time diverges.
D: measure of fragility related to depths and density in the minima in the potential energy landscape of the glass former.

Use of the Vogel–Fulcher equation allowed for fitting of the αβ merge region. Analysis using the V–F equation reveals the

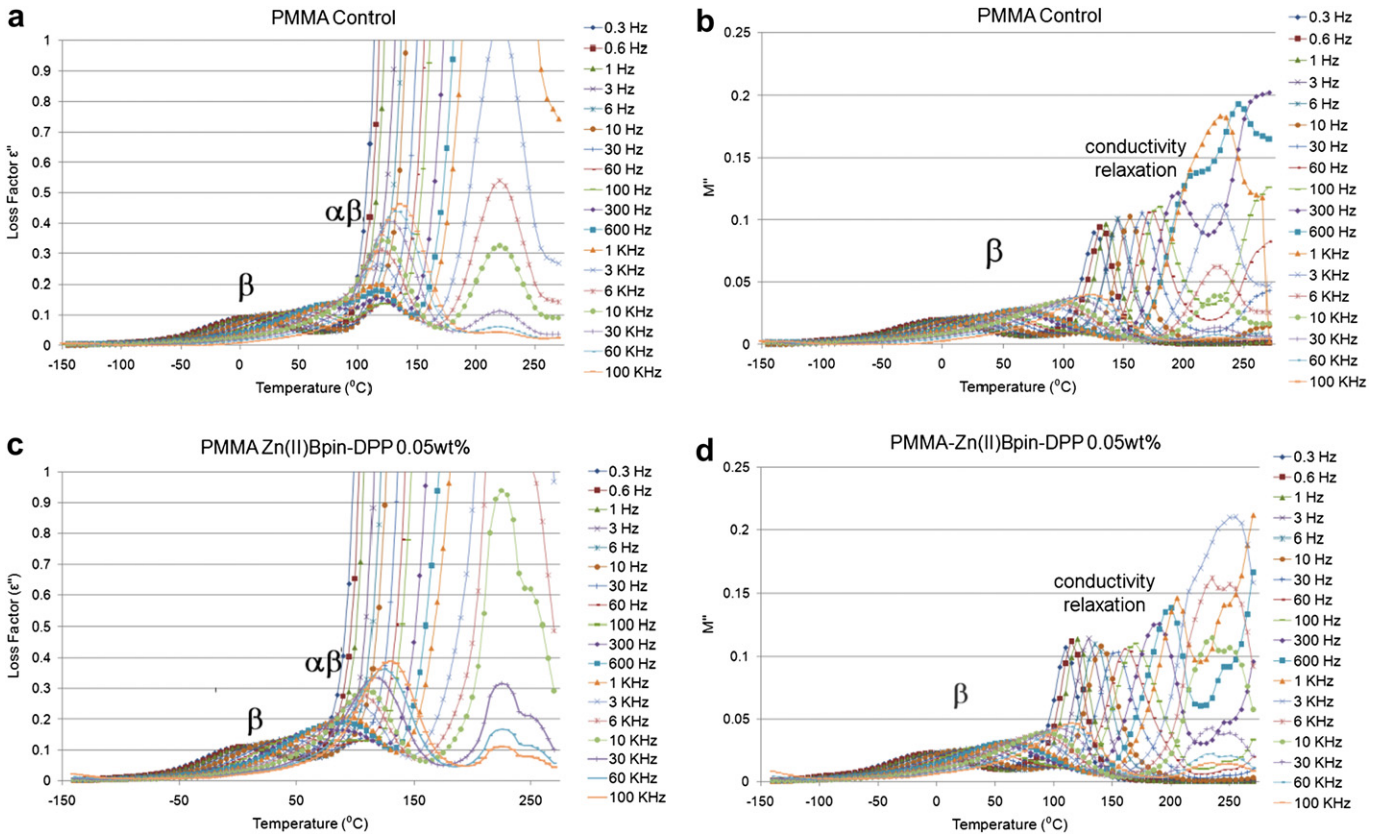

Fig. 7. (a and b) PMMA control loss factor (ε'') and electric loss modulus (M'') versus temperature (°C) plots, respectively. (c and d) PMMA-ZnBpin-DPP 0.05 wt% (w/w) plots of ε'' and M'' versus temperature (°C), respectively. β transitions are visible in all plots.

cooperative αβ merge to shift to lower T_0 temperatures (K) and τ_0 (s^{-1}) with increasing porphyrin content. Fig. 8a–d shows the V–F fitted plots using (eq. (7)), while Table 6 lists the V–F fitting parameters.

3.5. Unzipping of PMMA (thermal degradation)

In this study, samples were brought up to 270 °C for dielectric analysis to further DEA understanding of PMMA beyond the 190 °C, a common high temperature stop point in literature. The increased high temperature endpoint would allow for investigation of the thermal degradation of PMMA using DEA. In the temperature region of *ca.* 215–220 °C frequency independent maxima were observed for ε' and ε'' plots for all samples. The maxima of the loss modulus peaks, ε'', increased with decreasing frequency reaching a maximum peak height value at 0.3 Hz as shown in the ε'' plots in Fig. 9a and b. This temperature region is associated with the unzipping of PMMA and may represent individual monomer repeat units in the initial process of degradation. The temperature at which this occurs corresponds to the first of a two part thermal degradation process. This first process proceeds with the 'unzipping' or scission of individual monomer repeat units of the vinylidine chain ends, Scheme 1, a process that has been previously observed using thermogravametric analysis (TGA) and FTIR [53–55].

Frequency independent regions when voltage is held constant have been observed in DEA analysis of systems where components are in separate phases [56,57]. Coincidently, these regions look similar to goldstone relaxations. It should be noted that the goldstone relaxations occur from increasing applied voltage which then uncoils the polymer chain ultimately decreasing the loss modulus peak intensity [48,58]. Since the voltage in the TA 2970 is held constant, the observed frequency independent region is not of goldstone origin, but is caused by a phase change. These observations allow us to assign this area to the degradation process where the PMMA is unzipping, which regenerates the methyl methacrylate monomer (MMA). Upon degradation, the MMA monomer is then volatilized into the gas phase separating itself from the solid composite. The degradation process

Table 3
Comparison of ε'' (ω_{max}) and M'' (ω_{max}) peak maximums at 300Hz for PMMA and PMMA-Zn(II)Bpin-DPP composites. The two methods show that increasing porphyrin content trends maxima to lower temperatures (°C).

	β transition 300 Hz	
	ε'' (ω_{max}) (°C)	M'' (ω_{max}) (°C)
PMMA	69	56.67
0.05 wt%	65	52
0.11 wt%	65	52
0.9 wt%	61	49.3

Table 4
Comparison of apparent E_a of β relaxation using ε'' and M'' for PMMA and PMMA-Zn(II)Bpin-DPP composites.

	ε''		M''	
	E_a β (kJ mol^{-1})	E_a β (kcal mol^{-1})	E_a β (kJ mol^{-1})	E_a β (kcal mol^{-1})
PMMA	78.2	18.7	79.3	18.9
0.05 wt%	81.1	19.4	78.9	18.8
0.11 wt%	81.4	19.4	82.8	19.8
0.9 wt%	77.6	18.5	80.3	19.2

Table 5
Temperature (K) at $\varepsilon''(\omega_{max})$ αβ merge. Increasing porphyrin content trended lower $\varepsilon''(\omega_{max})$ temperatures.

$\varepsilon''(\omega_{max})$ αβ merge (K)						
	100 kHz	60 kHz	30 kHz	10 kHz	6 kHz	3 kHz
PMMA	408.1	404.2	398.2	393.2	391.2	390.2
0.05 wt%	405.7	398.2	390.9	382.8	381.2	373.5
0.11 wt%	403.2	396.2	390.9	383.3	380.2	376.4
0.9 wt%	395.6	391.9	387.1	380.6	378.4	376.3

onset temperature remained independent of Zn(II)Bpin-DPP content.

3.6. Viscoelastic to conductivity relaxation

Argand plots were created to track the viscoelastic to conductivity region. An Argand plot allows for the analysis of complex plane, or graphing with imaginary values. Specifically, Argand plots are the graphical representations of an imaginary axis (y ordinate) orthogonal to a real axis (x abscissa). In this case, the M'' (loss modulus) is the imaginary component plotted on the ordinate axis and the M' (electric modulus) is the real component plotted on the abscissa axis. From these plots, the dielectric strength, interfacial polarization present (electrode-sample), average relaxation time (τ), viscoelastic influence on mechanism of conduction, and ideality of the polymer ion translational properties can be determined. It should be noted that with Argand plots of M'' versus M', the low frequency measurements are on the left side of the semi-circle while the high frequency is on the right side.

As the samples were heated approaching Tg, it can be seen in Argand plots that the interfacial polarization from the electrode (non-origin intercept) lessens, Fig. 10a–c. Interfacial polarization manifests as a non-origin (0,0) intercept [28]. This physically means there is a barrier of electron flow from the electrode and the sample. The reduced interfacial polarization results from the increased free volume which facilitates improved relaxation times and lessens the current flow barrier between heterogeneous items.

As seen in Fig. 10b, a transition between viscoelastic and conductivity relaxation mechanisms begins to manifest At 60 °C. At temperatures higher than Tg, the viscoelastic effects upon conductivity are limited, as discussed below. However, at this temperature viscoelastic effects within the polymer are still observed. The character of the conduction mechanism changes as the temperature is increased. The split manifests in a low frequency (left side) and high frequency (right side) influence which is still a function of temperature. At lower temperatures (<Tg), a cooperative polymer-ion hopping mechanism is present [31]. That is, the relaxations of the PMMA are needed to allow the ions to translate. When the temperature is increased slightly above Tg, the mechanism of conduction changes to an ion translation type that has limited viscoelastic effects.

Since PMMA is amorphous, deep wells exist as barriers for the charge carrier ions to traverse. Therefore, the lower frequencies

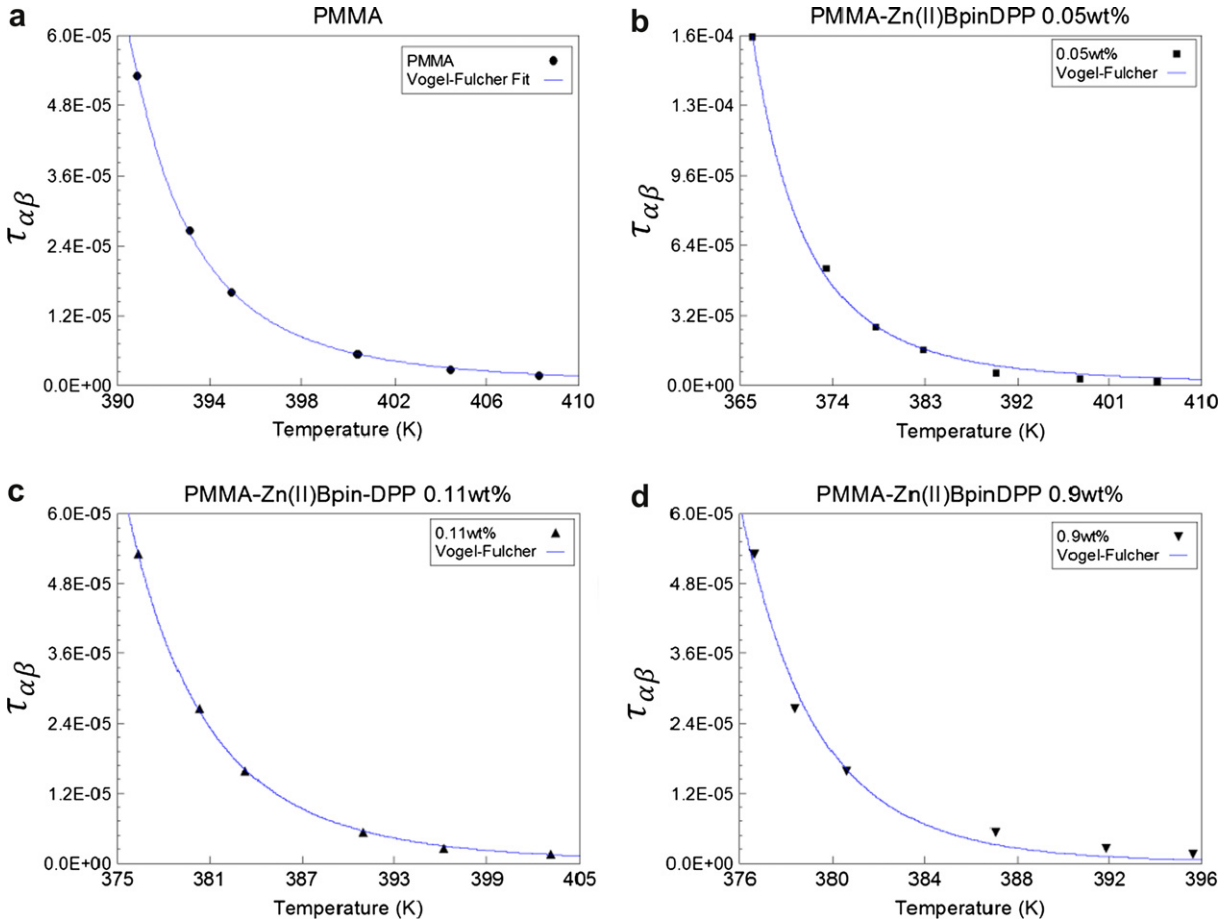

Fig. 8. (a–d) Vogel–Fulcher fitted $\tau_{\alpha\beta}$ relaxation times for the αβ merge region for (a) PMMA, (b) PMMA-Zn(II)Bpin-DPP 0.05 wt%, (c) PMMA-Zn(II)Bpin-DPP 0.11 wt%, and (d) PMMA-Zn(II)Bpin-DPP 0.9 wt%.

Table 6
Vogel–Fulcher fitting parameters for PMMA and PMMA-Zn(II)Bpin-DPP composites.

	T_0 (K)	τ_0 (s^{-1})	D	R^2
PMMA	369	2.76E − 08	0.450	0.999
0.05 wt%	325	6.01E − 08	1.000	0.9976
0.11 wt%	313	3.09E − 10	2.432	0.999
0.9 wt%	310	7.05E − 14	4.375	0.984

facilitate greater mean displacements to overcome the well barrier [31]. In Fig. 10c and d, there are two semicircles. The left most side (low frequency) has a greater semi-circle maximum due to longer mean displacement times facilitating greater ion flow. The right most side (high frequency) statistically will have less time to provide for mean displacement. Combining less mean displacement time with deep wells that trap a fraction of the charge carriers potentially explains the lower maxima seen. The low frequency semi-circle maximum is higher because lower frequencies have longer cycle times. This allows for greater mean displacement at lower frequencies.

At 105 °C, the addition of the Zn(II)Bpin-DPP porphyrin accelerates the transition into the conductivity relaxation, ion translation, mechanism over than that of the viscoelastic nature, polymer–ion interaction, Fig. 10c.

In Fig. 10d, PMMA-Zn(II)Bpin-DPP 0.9 wt% sample is shown and semicircles are added for visual aid for the low frequency conductivity relaxation mechanism (left side), and the high frequency viscoelastic conduction mechanism (right side). Note that the total conduction at these temperatures would still be described as combination of these two events which is represented by the outer semi-circle. In this region, there will be two predominate average relaxation times, τ, for each process.

As the temperature is increased, the viscoelastic effects are made negligible and the conductivity mechanism predominates in the sample. Fig. 11 shows at 155 °C only one arc is observed with a low frequency origin intercept, thus revealing a predominant conductivity relaxation.

3.6.1. Conductivity relaxation

Mathematically treating ε'' (loss factor) to obtain M'' (electric loss modulus) allows for the resolution of the viscoelastic process form the conductivity effects. Essentially, (eq. (5)) allows the space charge effects to be suppressed revealing the ionic conductivity peaks [16,22,27]. This separation reveals the conductivity relaxations (>Tg), $\alpha\beta$ merge, and a clarified simple β relaxation in terms of the electric loss modulus, M''. The α relaxation is not typically seen fully resolved in PMMA after the electric modulus formalism due to its weak intensity and cooperative $\alpha\beta$ merging that manifests.

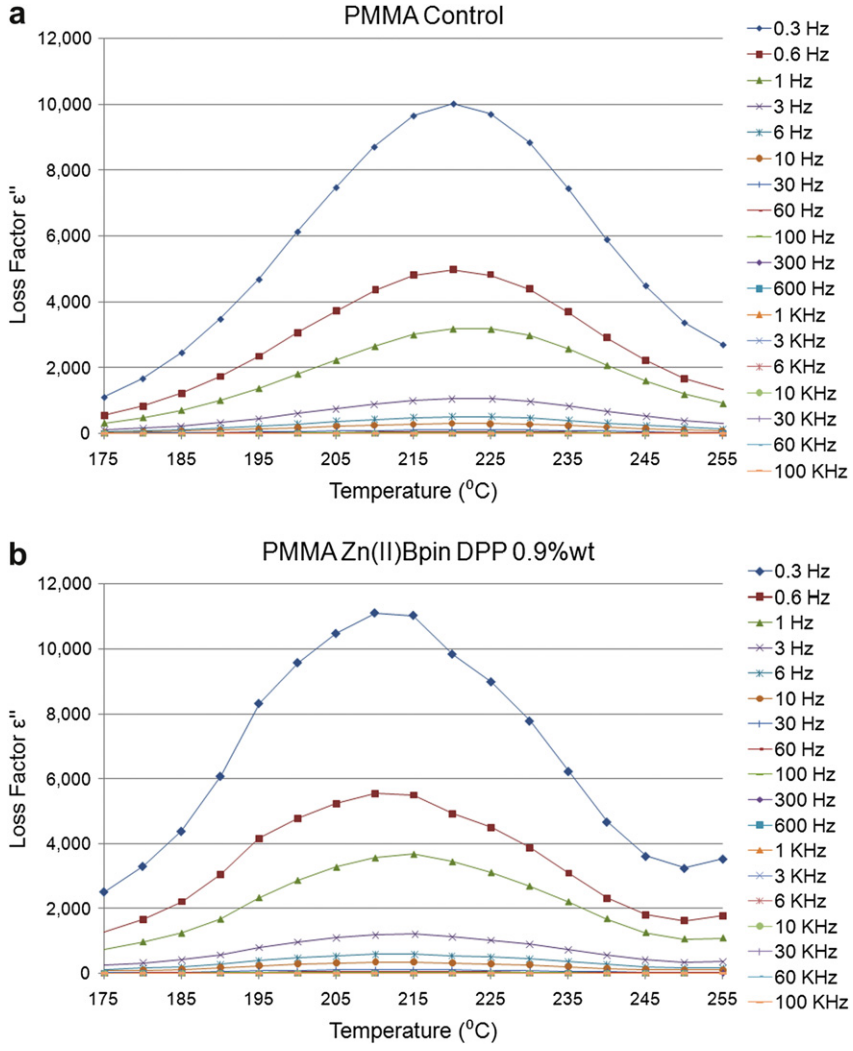

Fig. 9. Frequency independent region of ε'' (loss factor) versus temperature (°C) for (a) PMMA control and (b) PMMA0-Zn(II)Bpin-DPP 0.9 wt% samples.

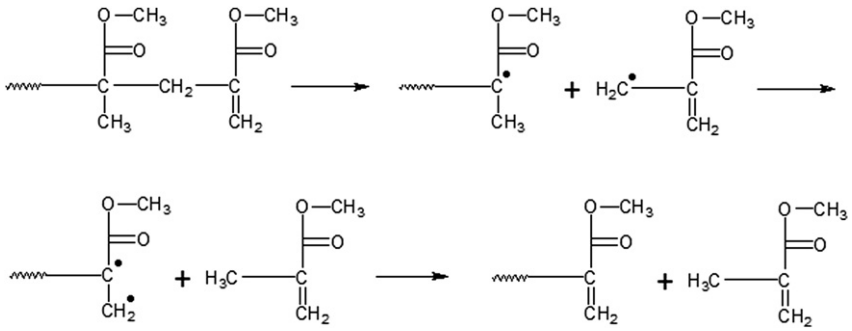

Scheme 1. Poly(methyl methacrylate) thermal degradation via end group scission.

Three proofs exist to confirm ionic conductivity relaxations [21,27,28]. The first proof, Argand plots demonstrate that viscoelastic effects from the polymer are minimized. The second proof is a comparison of our samples to ideal ionic translation. The last proof, AC conductivity, demonstrates no frequency dependence upon conductivity revealing true conductivity relaxations.

3.6.2. Proof 1 Argand plots

Dielectric permittivity, ε', and loss factor, ε'', can be explained using (eqs. (2) and (3)) for a single relaxation time. Cole and Cole [59] proposed that by plotting ε'' versus ε' at a particular temperature a semi-circle with a radius $(\varepsilon_R - \varepsilon_U)/2$ is obtained.

In M'' versus M' plots, values proceed from lower frequencies to higher frequencies. Semicircular behavior is characteristic of Debye behavior for small rigid molecules and molecular liquids [46,47]. When a semi-circle arc is observed in these plots, it indicates that viscoelastic relaxations are not present and only the effects from the conductivity relaxations are observed. The ideal semi-circle arc can be represented by the Debye semi-circle equation, (eq. (8)), when above the Tg of the polymer.

$$\left(M' - \left\{\frac{M_\infty - M_S}{2}\right\}\right)^2 + (M'')^2 = \left(\frac{(M_\infty - M_S)}{2}\right)^2 \tag{8}$$

M_∞: Electric Modulus at high frequency ($\omega \rightarrow \infty$)
M_S: Electric Modulus at zero frequency ($\omega \rightarrow 0$)

Polymers can deviate from this ideal behavior and exhibit skewed semicircles since they can have a distribution of relaxation times. Often due to this factor, polymers can be evaluated using

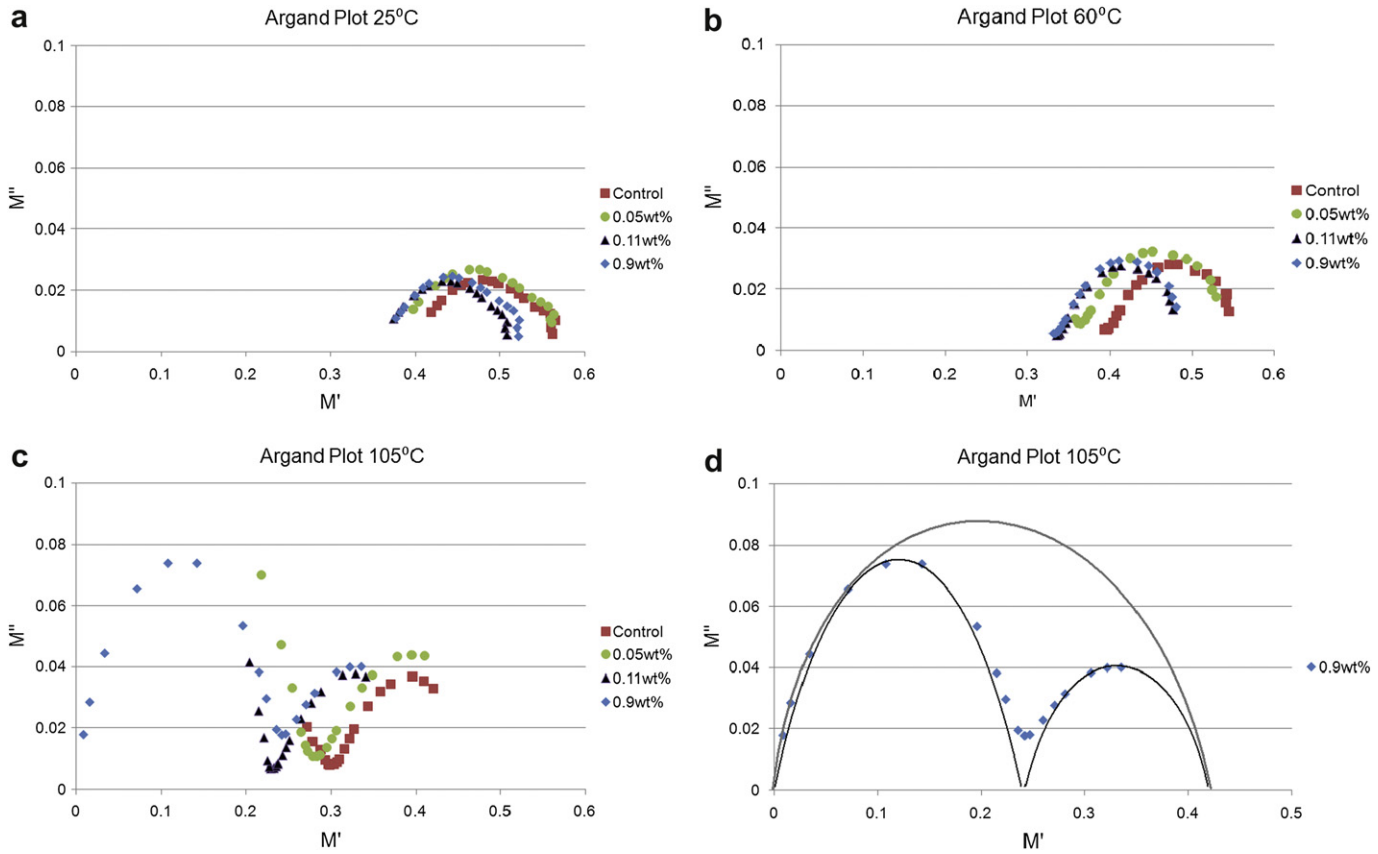

Fig. 10. Argand plots of M'' versus M' (a–c) PMMA Control and PMMA-Zn(II)Bpin-DPP composites in respective wt% (w/w) at 25, 60, and 105 °C, respectively. (d) PMMA-Zn(II)Bpin-DPP 0.9 wt% with overlaid semicircles for low, high, and combined low-high plots showing transition in conduction mechanism.

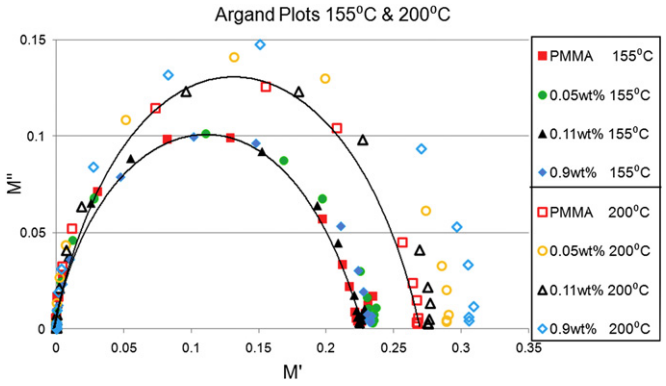

Fig. 11. Argand (complex plane) plots of M'' versus M' for temperatures 155 °C and 200 °C. Semicircle behavior denotes absence of viscoelastic effects. Semicircles shown in graph are a visual aide only.

a modified Debye equation: Cole–Cole (C–C), Cole–Davidson (C–D), or Havriliak–Negami (H–N) [30,59,60]. Fig. 11 shows an Argand (complex plane) plot of PMMA control and PMMA-Zn(II) Bpin-DPP composites at 155 °C and 200 °C. These plots exhibit semi-circle behavior within this region signifying the absence of viscoelastic relaxations.

From these Argand plots, the dielectric relaxation strength can be calculated using (eq. (9)). The dielectric relaxation strength is a measure of the alignment of dipoles within the sample and is listed in Table 7. All samples increased in dielectric strength with increasing temperature. The best dipole alignment occurs with the

Table 7
Dielectric relaxation strengths (ΔM) of samples tested.

Dielectric Strength (ΔM)			
	155 °C	180 °C	200 °C
PMMA	0.221	0.241	0.268
PMMA-Zn(II)Bpin-DPP 0.05 wt%	0.233	0.253	0.285
PMMA-Zn(II)Bpin-DPP 0.11 wt%	0.225	0.250	0.271
PMMA-Zn(II)Bpin-DPP 0.9 wt%	0.229	0.270	0.310

0.05 wt% sample at temperatures below 180 °C. At 180 °C, it appears that the added thermal energy allows for the 0.9 wt% sample to obtain higher alignment. Indicating that greater porphyrin content may be hindering the orientation of dipoles within the sample (below 180 °C), but still increases its overall conductivity (S/m) as discussed below. This presumably occurs as the enthalpy increase affords greater free volume within the sample allowing for better dipole reorientation to match the applied electric field. It remains unclear why the 0.11 wt% sample was anomalous to the macro trend, but we speculate on this later.

$$\Delta M = M_\infty - M_S \tag{9}$$

3.6.3. Proof 2 Log M″, M′ versus Log frequency

Starkweather et al. showed that at temperatures above the Tg when ε' (permittivity) is equal to ε_S (low frequency relaxed state) which is independent of temperature, there will be no contribution of viscoelasticity to ε'' (loss factor) having a conductivity of σ_0 (at a given temperature) [28]. Under these conditions, the complex permittivity, (eq. (1)), is given by the following (eq. (10))

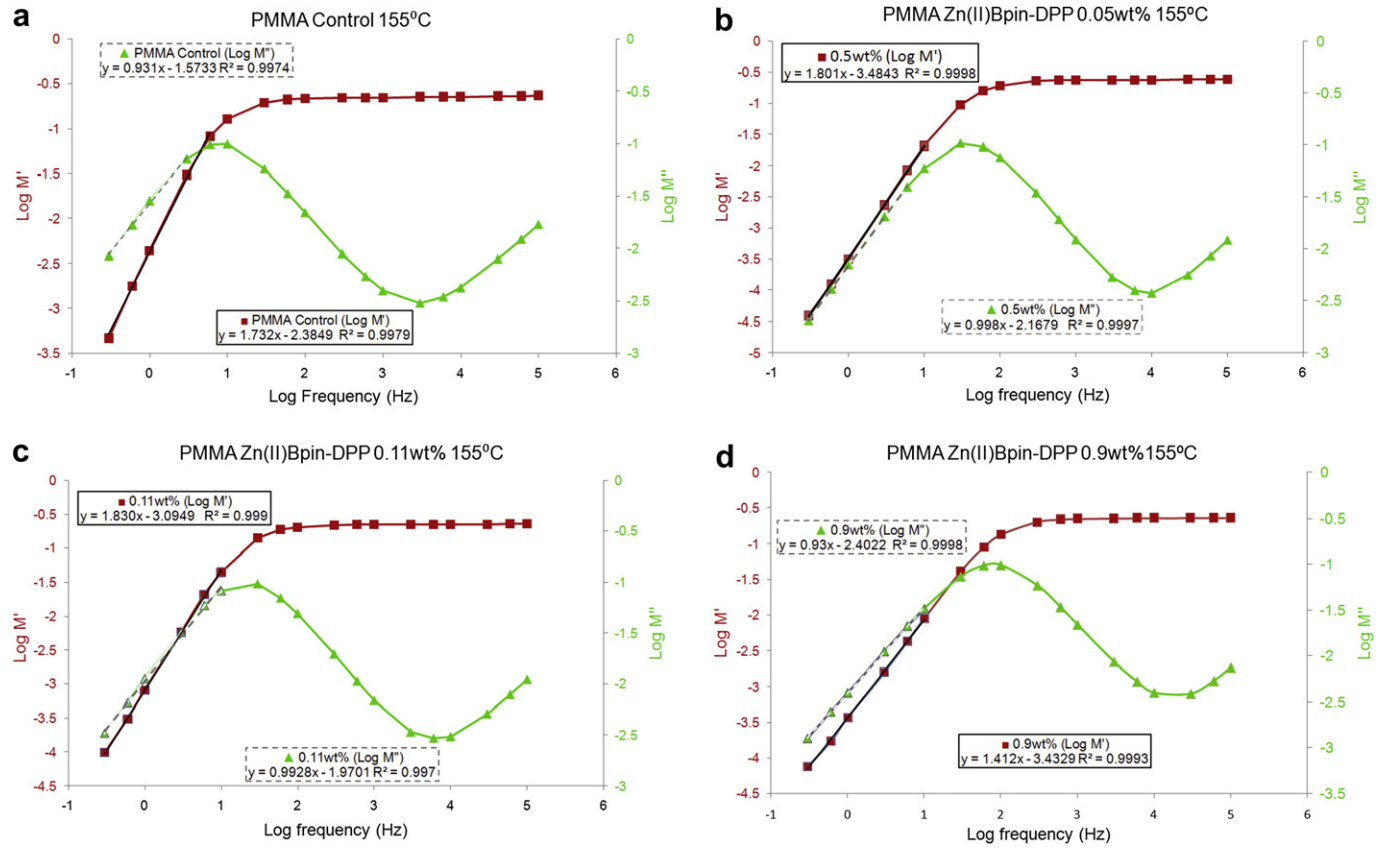

Fig. 12. (a–d) Log M' (■) and Log M''(▲) versus log frequency (Hz) plots for samples at 155 °C. Ideal slopes (m) for (■) and (▲) are 2 and 1, respectively.

$$\varepsilon^* = \varepsilon_S - \left(\frac{i\sigma_0}{\omega\varepsilon_0}\right) \tag{10}$$

ε^*: Complex permittivity
ε_S: Low frequency relaxed state ($\omega \rightarrow 0$)
ε_0: High Frequency unrelaxed state ($\omega \rightarrow \infty$)
ω: angular frequency ($2\pi f$)
σ_0: ionic conductivity

Starkweather et al. then applied this to the electric modulus in the following equations for M' and M''.

$$M' = M_S\left(\frac{\omega^2\tau_\sigma^2}{1+\omega^2\tau_\sigma^2}\right) \tag{11}$$

$$M'' = M_S\left(\frac{\omega\tau_\sigma}{1+\omega^2\tau_\sigma^2}\right) \tag{12}$$

where the characteristic time, τ_σ, and an electric modulus M_S are defined as:

$$\tau_\sigma = \frac{\varepsilon_0\varepsilon_S}{\tau_0} \tag{13}$$

$$M_S = \frac{1}{\varepsilon_S} \tag{14}$$

In plots of log M' versus log frequency, (eq. (11)) will exhibit an ideal slope of 2; and in plots of log M'' versus log frequency (0.3 Hz–1000 Hz) (eq. (11)) will exhibit an ideal slope of 1. Fig. 12a–d shows that all samples approach the ideal values of 2 or 1 respectively, confirming the start of the conductivity region (absence of viscoelastic effects) at 155 °C proving the observed relaxations are due to ionic conductivity.

3.6.4. Proof 3 AC conductivity

When viscoelastic effects are negligible, the loss factor is described by (eq. (4)). With algebraic manipulation AC conductivity (σ_{AC}) can be obtained (eq. (15)). Fig. 13a–d shows that in plots of σ_{AC} versus the log of frequency (Hz) for temperatures above Tg, conductivity is predominant for our samples.

$$\sigma_{AC} = \varepsilon''\omega\varepsilon_0 \tag{15}$$

It is understood that σ_{AC} is the sum of all dissipative effects including DC conductivity (σ_{DC}) caused by the translation of ions as well as the dielectric loss dispersions [61].

Increasing the frequency results in a mean displacement of the charge carriers, and after a critical frequency (f_c) the real part of conductivity follows a power law relationship at a constant temperature, (eq (15)) [61,62].

$$\sigma_{AC}(\omega) = \sigma_{DC} + A\omega^S \tag{16}$$

where σ_{DC} is the conductivity (S/m) as $\omega \rightarrow 0$, and A and s ($0 \le s \le 1$) are parameters that depend upon temperature, morphology, and composition [61,62].

As the temperature is increased σ_{AC} begins to show a plateau (*ca.* 155 °C) from 10^{-1} to 10^3 Hz, signifying the beginning of the conductivity relaxation region. The σ_{AC} plateau then expands to

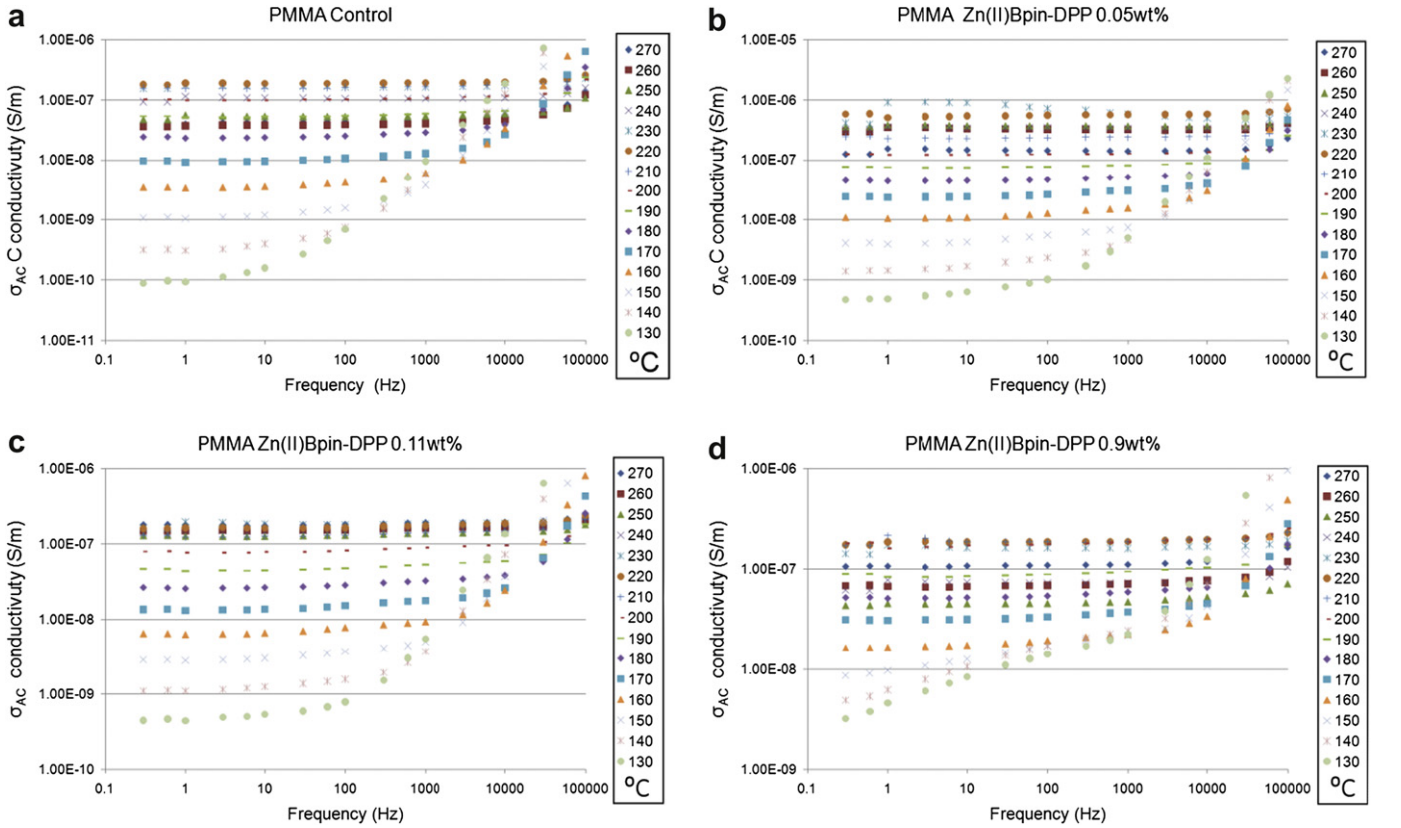

Fig. 13. (a–d) AC conductivity (σ_{AC}) (S/m) versus frequency (Hz): in temperature range of 130–270 °C (a) PMMA control. (b) PMMA-Zn(II)Bpin-DPP 0.05 wt% (w/w). (c) PMMA-Zn (II)Bpin-DPP 0.11 wt% (w/w). (d) PMMA-Zn(II)Bpin-DPP 0.9 wt% (w/w).

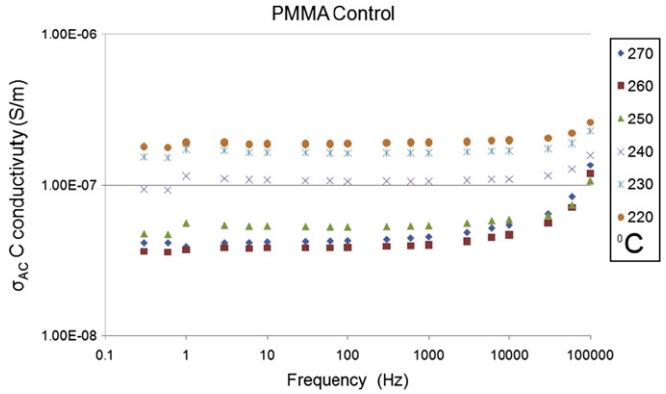

Fig. 14. PMMA Control: σ_{AC} (S/m) versus log frequency (Hz). σ_{AC} decreased in all samples *ca.* 220–270 °C.

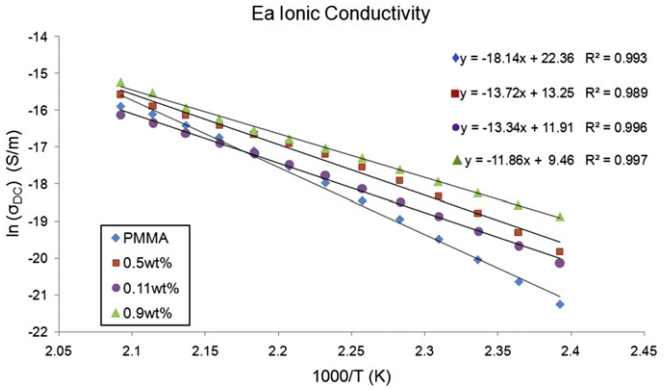

Fig. 16. ln σ_{DC} versus inverse temperature (K) plots of PMMA Control and PMMA-Zn(II) Bpin-DPP composites (0.05 wt%, 0.11 wt%, and 0.9 wt%).

include higher frequencies 10^3 to 10^6 Hz as the temperature is increased, thus the illustrating frequency independent conductivity relaxation region. The absence of the frequency dependence upon conductivity is the observation that signifies negligible viscoelastic effects. The low frequency plateau begins in the low frequency regime first because the alternating field provides sufficient time for charge carriers to translate over larger distances. As the temperature is increased, the higher frequency alternating fields begin to achieve an almost constant value joining the plateau. This analysis reveals the conductivity relaxation region to exist between 155 and 200 °C. Samples containing Zn(II)Bpin-DPP had approximately 15 times higher σ_{AC} values than that of the control PMMA.

3.7. AC conductivity decomposition region

With all samples, σ_{AC} increased with temperature up to *ca.* 220 °C. At this temperature, the σ_{AC} values decreased slightly presumably due to the decomposition of PMMA to MMA where phase separation occurs and presumably leads to a disruption of ionic flow. Fig. 14 illustrates the decreasing σ_{AC} conductivity.

3.8. DC conductivity

DC conductivity (σ_{DC}) was obtained by extrapolation to zero frequency. This may be accomplished either by solving (eq. (16)) for σ_{DC}, or following the convention of using the lowest frequency tested (<1 Hz) as the *y*-axis intercept when $\omega \rightarrow 0$ [61,62]. Choosing the latter is only applicable when the low frequency end (*ca.* 10^{-1} to 10^3 Hz) has maintained a plateau. If these lower frequencies curve downward then sample heterogeneity or interfacial polarization between the sample and electrode are present and (eq. (16)) should be utilized.

σ_{DC} follows the Arrhenius relationship shown in (eq. (17)) where σ_{DC} increased with increasing temperature and increasing Zn(II)Bpin-DPP content. Fig. 15 shows the relationship of σ_{DC} versus temperature for all samples within the conductivity region. Again the PMMA-Zn(II)Bpin-DPP 0.11 wt% sample is anomalous with the respect to the maxima σ_{DC} values, mirroring the dielectric strength. The reason for this is not understood, however it is speculated that this observation may be related to percolation theory as applied to polymers in a conductive environment.

$$\ln\sigma_{DC} = \ln\sigma_0 - \left(\frac{E_a}{RT}\right) \tag{17}$$

E_a: Activation Energy
R: Ideal gas constant
σ_{DC}: DC conductivity
σ_0: Pre-exponential factor (conductivity at infinite temperature)

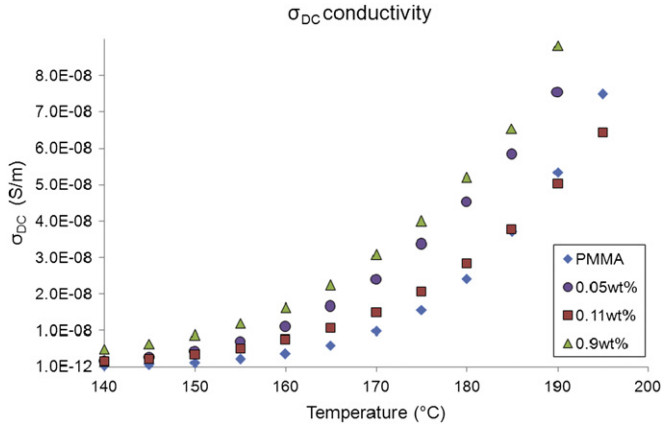

Fig. 15. σ_{DC} conductivity (S/m) versus temperature (°C) for PMMA, PMMA-ZnBpin-DPP 0.05 wt%, PMMA-ZnBpin-DPP (0.11 wt%), and PMMA-ZnBpin-DPP (0.9 wt%).

Ionic conductivity activation energies were obtained using plots of ln σ_{DC} versus inverse temperature (140–210 °C); Fig. 16 shows the plots for PMMA control and PMMA-Zn(II)Bpin-DPP composites. Activation energies decreased with increasing wt% of porphyrin. The addition of the Zn(II)Bpin-DPP lowered the E_a σ_{DC} from 150.8 to 98.1 kJ mol^{-1} (36–23.4 kcal mol^{-1}). This conforms to previous studies which have reported neat PMMA E_a σ_{DC} values of 54.3–152 kJ mol^{-1} (12.9–36.3 kcal mol^{-1}) [19,20,29]. E_a σ_{DC} values are presented in Table 8.

Table 8
Ionic conductivity activation energies (E_a) for PMMA and PMMA-Zn(II)Bpin-DPP composites. E_a σ_{DC} decreased with increasing Zn(II)Bpin-DPP content.

E_a σ_{DC}	kcal mol^{-1}	kJ mol^{-1}
PMMA	36.0	150.8
0.05 wt%	28.0	117.3
0.11 wt%	26.1	109.4
0.9 wt%	23.4	98.1

4. Conclusion

Optically transparent composite films were made of PMMA and Zn(II)Bpin-DPP then analyzed via DEA, DSC, and UV–vis.

Calculation of the dipole of Zn(II)Bpin-DPP was found to be 2.87 Debye on an optimized structure. The vector points from the Zn center to the boron-containing substituent.

Permittivity of the PMMA composites increased with increasing porphyrin content and further increased with increasing temperature. This increase in permittivity had a maximum limit beyond which no additional increase was observable beyond 0.11 wt% of Zn (II)Bpin-DPP loading.

DSC showed that Zn(II)Bpin-DPP acted as an antiplasticizer increasing the Tg with increasing wt%.

The αβ merge was shown to shift to lower temperatures with the increased loading of porphyrin. The employment of the electric modulus formalism allowed for the separation of viscoelastic and conductivity relaxations. This allowed for the study of the effects of increased loading of Zn(II)Bpin-DPP on β and conductivity relaxations. The β relaxation showed no appreciable change in apparent activation energy E_a. The conductivity relaxation showed a decrease in apparent activation energy, E_a.

The conductivity region (155–200 °C) was confirmed through three proofs. AC conductivity, σ_{AC}, was shown to increase in all samples with increasing temperature. Increasing wt% of porphyrin effected σ_{AC} showing an increase in conductivity, up to 15 times greater over the PMMA control.

With the exception of the PMMA-Zn(II)Bpin 0.11 wt% sample, σ_{DC} and dielectric strength increased with increasing temperature and increasing wt% of porphyrin. However, the E_a σ_{DC} calculated values followed the trend of decreasing the activation energy with increasing Zn(II)Bpin-DPP content. Since only the PMMA-Zn(II) Bpin-DPP 0.11 wt% had exceptions relating to ion translation, it is speculated that percolation theory with respect to charge carrier motion may explain such observations.

This study is believed to be the first to inspect the first part of degradation of PMMA using DEA. A frequency independent region was observed around 220 °C. This correlates with the degradation of the PMMA into MMA monomer repeat units. The phase separation of the polymer and gaseous MMA is believed to be the source of the frequency independent region. σ_{AC} was observed to decrease in this unzipping region most likely a result of the disruption of ionic carrier flow through the samples due to phase separation.

Additionally, this composite offers interest in electrical applications since the added porphyrin uniquely raises the Tg affording improved thermal stability while simultaneously making ion translation easier. Further investigation by dynamic mechanical analysis and fluorescence spectroscopy could lead to a better understanding of the antiplastization effects provided by Zn(II)Bpin-DPP.

Future work will focus upon evaluating the conductivity regions via Haveriliak–Negami analysis to further evaluate central (average) relaxation times, τ.

Acknowledgements

We would like to thank Kari Fowler of Georgia Pacific Atlanta Georgia USA for supplying material support of our continued research in dielectric analysis. We extend our thoughts and prayers to her family. This research was made possible through funding from the Department of Defense under grant HDTRA1-08-0035.

References

[1] Chen Y, Zhang XP. J Org Chem 2003;68(11):4432–8.
[2] Gao G-Y, Chen Y, Zhang XP. J Org Chem 2003;68:6215–21.
[3] Gao G-Y, Colvin AJ, Chen Y, Zhang XP. Org Lett 2003;5:3261–4.
[4] Gao G-Y, Chen Y, Zhang XP. Org Lett 2004;6:1837–40.
[5] Gao G-Y, Colvin AJ, Chen Y, Zhang XP. J Org Chem 2004;69:8886–92.
[6] Chen Y, Gao G-Y, Zhang XP. Tetrahedron Lett 2005;46:4965–9.
[7] Gao G-Y, Ruppel JV, Allen B, Chen Y, Zhang XP. J Org Chem 2007;72 (24):9060–6.
[8] Ruppel JV, Jones JE, Huff CA, Kamble RM, Chen Y, Zhang XP. Org Lett 2008;10 (10):1995–8.
[9] Zhu S, Ruppel JV, Lu H, Wojtas L, Zhang XP. J Am Chem Soc 2008;130 (15):5042–3.
[10] Fields KB, Ruppel JV, Snyder N, Zhang XP. Handbook of porphyrin science. In: Kadish KM, Smith KM, Guilard R, editors. Advances in synthesis and coordination chemistry of porphyrins, Phthalocyanines and Related Systems, vol. 3. Hackensack, NJ: World Scientific; 2010. p. 367–428 [Chapter 13].
[11] Gedde UW. Polymer physics. New York: Chapman & Hall; 1999.
[12] TA instruments, DEA 2790 dielectric analyzer, TA-057, TA instruments applications library, www.tainst.com.
[13] Garwe F, Schonhals A, Lockwenz H, Beiner M, Schroter K, Donth E. Macromolecules 1996;29:247–53.
[14] Williams ML, Landel RF, Ferry JD. J Am Chem Soc 1955;77:3701–7.
[15] Leon C, Ngai KL, Roland CM. J Chem Phys 1999;110(23):11585–91.
[16] Kim MS, Sekhar PK, Bhansali S, Harmon JP. J Nanosci Nanotechnol 2009;9:1–9.
[17] Tatro SR, Baker GR, Bisht K, Harmon JP. Polymer 2003;44:167–76.
[18] Mai C, Johari GP. J Polym Sci Part B Polym Phys 1897;25:1903–11.
[19] Clayton LM. The design, fabrication, and characterization of polymer–carbon nanotube composites. Ph.D. thesis, University of South Florida; 2005.
[20] Clayton LM, Knudsen B, Cinke M, Meyyappn M, Harmon JP. J Nanosci Nanotechnol 2007;7(10):3572–9.
[21] McCrum NG, Read BE, William G. An elastic and dielectric effects in polymeric solids. New York: John Wiley & Sons; 1967.
[22] Mohomed K, Gerasimov TG, Moussy F, Harmon JP. Polymer 2005;46: 3847–55.
[23] Mohomed K, Moussy F, Harmon JP. Polymer 2006;47:3856–65.
[24] Clayton LM, Sikder AK, Kumar A, Cinke M, Meyyappan M, Gerasimov TG, et al. Adv Funct Mater 2005;15(1):101–6.
[25] Bergman R, Alverez F, Alegri A, Colmenero J. J Chem Phys 1998;109 (17):7546–55.
[26] Wang CJ, Huang YN, Zhang WX, Guzmon J, Nogales A, Ezguerra T, et al. Phys Status Solidi 2002;193(2):357–66.
[27] Ambrus JH, Moynihan CT, Macedo PB. J Phys Chem 1972;76(22):3287–95.
[28] Starkweather Jr HW, Avakian P. J Polym Sci Part B Polym Phys 1992;30:637–41.
[29] Mohomed K, Gerasimov TG, Abourahma H, Zaworotko MJ, Harmon JP. Mater Sci Eng A 2005;409:227–33.
[30] Havriliak S, Negami S. J Polym Sci Part C 1996;14:99–117.
[31] Muddarra M, Diaz-Calleja R, Belana J, Canadas JC, Diego JA, Sellares J, et al. Polymer 2004;45:2737–42.
[32] Gomez Ribelles JL, Diaz Calleja R. J Polym Sci Part B Polym Phys 1985;23:1297–307.
[33] Higgenbotham-Bertolucci PR, Gao H, Harmon JP. Polym Eng Sci 2001;41 (5):873–80.
[34] Nogueira AF, Longo C, De Paoli MA. Coord Chem Rev 2004;248 (13–14):1455–68.
[35] Chen Y, Fields KB, Zhang XP. J Am Chem Soc 2004;126(45):14718–9.
[36] Gao G-Y, Ruppel JV, Fields KB, Xu X, Chen Y, Zhang XP. J Org Chem 2008;73 (13):4855–8.
[37] Yoon M-C, Choo S, Kim P, Hori T, Aratani N, Osuka A. J Phys Chem B 2009;113:15074–82.
[38] Satake A, Kobuke Y. Org Biomol Chem 2007;5:1679–91.
[39] Hyslop AG, Kellet MA, Iovine PM, Therien MJ. J Am Chem Soc 1998;120 (48):12676–7.
[40] Frisch MJ, Trucks GW, Schlegel HB, Scuseria GE, Robb MA, Cheeseman JR, et al. Gaussian 03, Revision C.02. Wallingford CT: Gaussian, Inc.; 2004.
[41] Catlett C. TeraGrid: analysis of organization, system architecture, and middleware enabling newtypes of applications. HPC and Grids in Action. Amsterdam: IOS Press; 2007.
[42] Schmidt MW, Baldridge KK, Boatz JA, Elbert ST, Gordon MS, Jensen JH, et al. J Comput Chem 1993;14:1347–63.
[43] Zhao Y, Truhlar DG. Theor Chem Acc 2008;120:215–41.
[44] Truhlar DG, Zhao Y. Acc Chem Res 2008;41:157–67.
[45] Marsh DF, Mink LM. J Chem Educ 1996;73(12):1188–90.
[46] Debye P. Phys Z 1912;13:97–100.
[47] Debye P. Chem Rev 1936;19(3):171–82.
[48] Runt JP, Fitzgerald JJ, editors. Dielectric spectroscopy of polymeric materials fundamentals and applications. Washington D.C.: American Chemical Society; 1997. p. 7–8.
[49] Maxwell JC. Electricity and magnetism. V1. Oxford: Clarendon; 1892. p. 452.
[50] Wagner KW. Arch Elektrotech 1914;2:371.
[51] Sillars RW. J Inst Elect Eng 1937;80:378.
[52] Angel CA. J Res Natl Inst Stan 1997;120(2):171–84.
[53] Kashiwagi T, Inaba A, Brown JE, Hatada K, Tatsuki K, Msuda E. Macromolecules 1986;19(8):2160–8.
[54] Ganesh K, Latha R, Kishore K, George B, Ninan KN. J Appl Polym Sci 1997; 66:2149–56.

[55] Wilkie C. Polym Degrad Stab 1999;66:301–6.
[56] Emran SK, Liu Y, Newkome GR, Harmon JP. J Polym Sci Part B Polym Phys 2001;39:1381–93.
[57] Nguyen LH, Gu M. Macromol Chem Phys 2005;206:1659–64.
[58] Vallerien SU, Kremer F, Kapitza H, Zentel R, Frank W. Phys Lett A 1989;138 (5):212–22.
[59] Cole KS, Cole RH. J Phys Chem 1941;9:341–51.
[60] Davidson DW, Cole RH. J Chem Phys 1950;18:1417–8.
[61] Kalgaonkar RA, Jog JP. J Polym Sci Part B Polym Phys 2008; 46:2539–55.
[62] Tsangaris GM, Psarras GC, Manolakaki E. Adv Comput Lett 1999; 8(1):25.